Thermofluid-Dynamic Assessment of the EU-DEMO Divertor Single-Circuit Cooling Option

A. Quartararo[a,*], S. Basile[a], F.M. Castrovinci[a], P.A. Di Maio[a], M. Giardina[a], G. Mazzone[b], E. Vallone[a], J.H. You[c]

[a] *Department of Engineering, University of Palermo, Viale delle Scienze, Ed. 6, 90128 Palermo, Italy*
[b] *Department of Fusion and Technology for Nuclear Safety and Security, ENEA C. R. Frascati, via E. Fermi 45, 00044 Frascati (Roma), Italy*
[c] *Max Planck Institute of Plasma Physics (E2M), Boltzmann Str.2, 85748 Garching, Germany*

Abstract

Until 2019, the thermo-hydraulic development of the EU-DEMO divertor was based on the "double-circuit" concept, in which two independent cooling circuits served by two different Primary Heat Transfer Systems were used to cool the Plasma-Facing Components (PFC) and the Cassette Body (CB). During the Divertor Final Design Review Meeting, held in May 2020, the possibility to adopt a single cooling circuit to serve both components was suggested. This new cooling circuit was originally conceived with the aim of simplifying remote maintenance, with potential benefits for some aspects of safety and balance of plant design and integration. During the years from 2020 to 2022, in the framework of the Work Package DIV 1 - "Divertor Cassette Design and Integration" of the EUROfusion action, University of Palermo and ENEA carried out a research campaign focussed on the preliminary thermofluid-dynamic assessment of this new concept, highlighting its strengths and weaknesses. The research campaign was carried out following a theoretical-computational approach based on the finite volume method and adopting the commercial computational fluid-dynamic code ANSYS-CFX. The steady-state thermal-hydraulic performances of the single-circuit DEMO divertor concept were assessed in terms of coolant pressure drop and flow velocity distribution, mainly in order to check coolant aptitude to provide a uniform and effective cooling to CB, shielding liner, reflector plates, PFCs and the newly introduced neutron shields to improve the shielding of the vacuum vessel. Moreover, the margin against critical heat flux distributions among the plasma-facing channels were assessed by adopting appropriate correlations, to check the compliance with the applicable constraints. Models, loads and boundary conditions assumed for the analyses are herewith reported and critically discussed, together with the main results obtained.

Keywords: DEMO, Divertor, Plasma facing components, Thermofluid-dynamics, CFD analysis

1. Introduction

The divertor is a critical in-vessel component of nuclear fusion reactors, being responsible for the fulfilment of certain fundamental functions for the machine. In fact, it must be able to handle the power deposited by charged particle and neutron irradiation, ensure the presence of channels through which the fusion ashes can be removed from the Vacuum Vessel (VV), provide plasma-compatible surfaces, and shield the VV and magnets from nuclear loads [1].

Its importance is emphasised by the "European Research Roadmap to the Realisation of Fusion Energy", which defines reliable power exhausting as one of the main challenges in the realization of a Fusion Power Plant (FPP) [2]. Moreover, the heat load that can be tolerated by the divertor under normal and off-normal operating conditions is a pivotal parameter when dimensioning an FPP [3].

A proper design of its cooling circuit allows the divertor to accomplish its mission of handling the surface heat loads, preventing structural and functional materials to operate outside their operative limits, while avoiding unduly high pressure drops and operating at the highest possible temperature to ensure the maximum achievable thermodynamic cycle efficiency.

During the Pre-Conceptual Design (PCD) phase, which ended in 2020 [4], attention was focussed on the study of a "Double-Circuit" divertor concept, in which two independent cooling circuits served by two differ-

*Corresponding author
Email address: andrea.quartararo@unipa.it (A. Quartararo)

ent Primary Heat Transfer Systems were used to cool the Plasma-Facing Components (PFC) and the Cassette Body (CB) [1].

To ease the remote maintenance while allowing for a simpler balance of plant design, during the PCD Divertor Final Design Review Meeting it was suggested to adopt a single cooling circuit for both PFC and CB. This has led to the definition of a new divertor concept, namely Configuration 2021 or "Single-Circuit Cooling Option" [5].

During the years from 2020 to 2022, within the EUROfusion Work Package DIV 1 - "Divertor Cassette Design and Integration", a research campaign focussed on the preliminary thermofluid-dynamic assessment of this new concept has been carried out as a joint activity between University of Palermo and ENEA, with the aim of verifying its compliance with constraints on minimum Critical Heat Flux (CHF) margin for the PFCs, total pressure drop, and capacity to provide a uniform and effective cooling of the structures.

The research campaign was performed following a theoretical-numerical approach based on the finite volume method and adopting the ANSYS CFX 2021 R1 commercial Computational Fluid-Dynamic (CFD) code [6].

Models, loads and boundary conditions assumed for the analyses are herewith reported and critically discussed, together with the main results obtained.

2. Outline of Single-Circuit Cooling Option DEMO divertor cassette

The DEMO divertor, according to the current design, is articulated in 48 toroidal cassettes. Each cassette is composed of a CB supporting two Reflector Plates (RP), a Shielding Liner (SL), the PFCs, namely the Inner and Outer Vertical Targets (IVT and OVT), and two Neutron Shields (NS). The latter ones are located inside the vacuum pumping hole and introduced in order to improve the shielding of the Vacuum Vessel (VV) against neutron loads. The sketch of the cassette geometry and all supported components is depicted in fig. 1.

During normal and off-normal operating conditions of the divertor, the cassettes will be subjected to surface and volumetric thermal loads. The removal of this power relies on the adoption of subcooled pressurised water as a coolant, the operating conditions of which, with particular reference to the cooling circuit layout configuration under investigation, are still under discussion.

The integration of the PFC and CB cooling circuits, together with the inclusion of the NS, leads to a significant increase in the complexity of the cooling circuit layout. The flow routing is depicted in fig. 2, showing how the individual components supported by the CB are themselves cooled by a rather complex system of cooling channel arrays arranged in series and parallel to each other. Additionally, the cooling scheme be schematised as shown in fig. 3 with reference to the component nomenclature depicted in fig. 4.

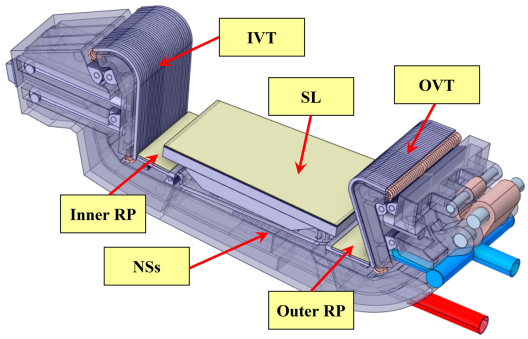

Figure 1: DEMO divertor cassette (Single-cooling circuit option).

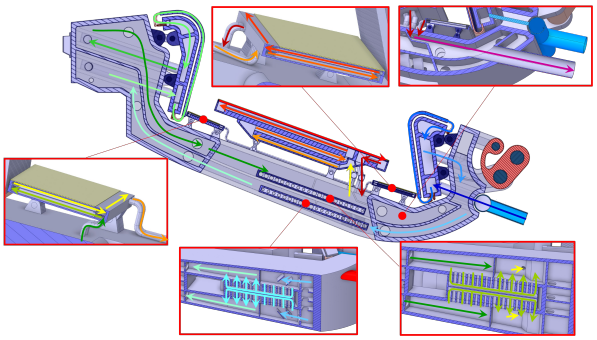

Figure 2: DEMO single-circuit cooling option divertor cassette flow routing.

As far as the two VTs are concerned, these consist of Plasma Facing Units (PFUs), whose design is inspired by the ITER tungsten monoblock concept [7] and whose geometrical features, together with the details of their connections with the supporting bodies are thoroughly reported in [1]. The PFUs are grouped in toroidally-arranged PFU assemblies, 46 and 34 respectively for OVT and IVT, each one consisting of a longitudinal array of PFUs connected by a cooling pipe made of CuCrZr alloy, running through the centre bore of the monoblocks. The PFU assemblies are mounted on dedicated bodies, namely Target Bodies (TB), fixed

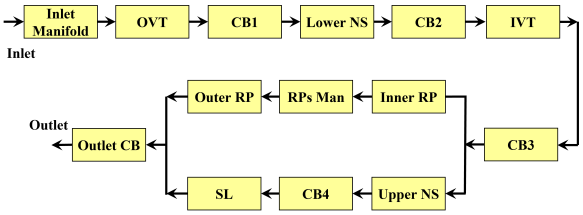

Figure 3: DEMO single-circuit cooling option divertor cassette cooling scheme.

to the CB by an ITER-like multi-link fixation system [5], while their cooling pipes are equipped with copper swirl tape turbulence promoters and are joined to the tungsten blocks with a thin copper interlayer.

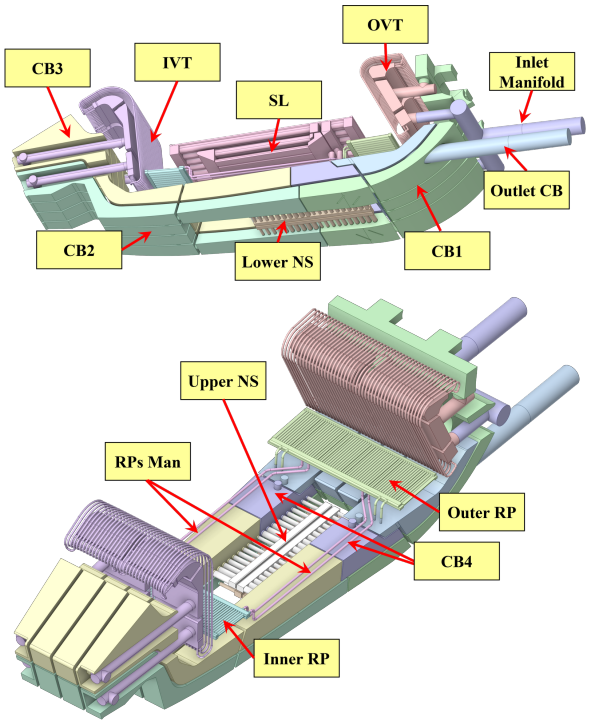

Figure 4: DEMO single-circuit cooling option divertor cooling circuit main components.

Regarding the SL, it consists of a Eurofer structure armoured by a 2 mm tungsten coating on the surface exposed to the plasma. Its cooling circuit consists of four levels of channels running along the radial direction, in series with each other, and each level in turn consists of several channels arranged in parallel. According to the 2021 configuration, the water is first routed to three levels of Back Channels (BC), characterized by a large cross-section so to ensure a sufficient volume of water to fulfil cooling and neutron moderation functions. The coolant is then fed to 53 toroidally-parallel First Wall (FW) channels, positioned a few millimetres from the surface exposed to the plasma, designed to handle the expected heat fluxes, and finally conveyed back to the cassette. Figure 5 shows the layout of the the SL cooling circuit, as well as the adopted nomenclature for the channels.

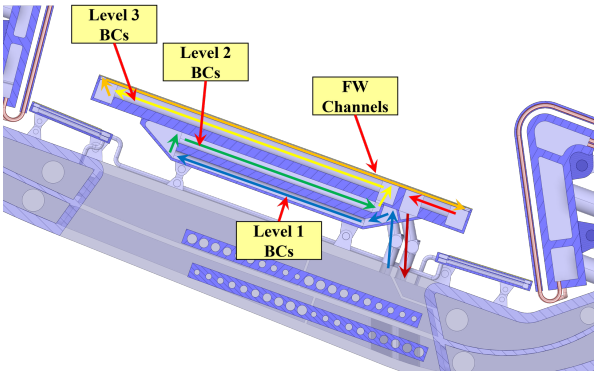

Figure 5: Details of flow routing inside the SL and channel nomenclature.

As for the RPs, these are, like the SL, Eurofer structures with a tungsten coating on the surfaces exposed to the plasma. Their cooling circuit is composed of one level of BC and one level of FW channels, the latter being 61 and 49 for the outer and inner RPs (ORP, IRP) respectively.

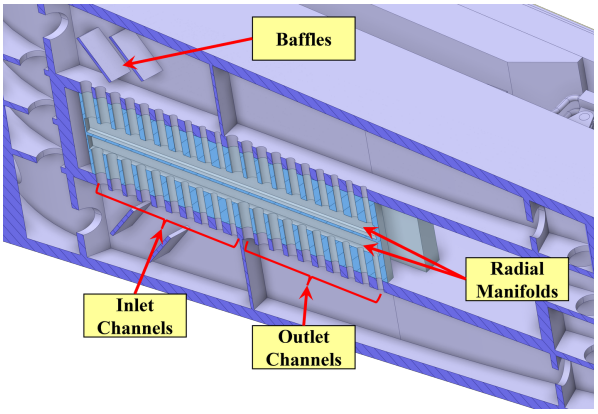

Figure 6: DEMO single-circuit cooling option divertor cassette cross-section showing the lower NS coolant distribution details (NSs are depicted in light blue).

Finally, with reference to the NSs, these consist of two Eurofer plates positioned inside the vacuum pumping hole and connected directly to the cooling circuit

of the cassette, namely upper and lower NSs. For each NS, there are two separated cooling circuits, each one consisting of an array of 10 inlet and 10 outlet channels arranged in a toroidal direction, interconnected by a radial manifold, as shown in fig. 6. As can be seen, the diameter of the channels is variable along the radial direction, as a result of a preliminary fluid-dynamic optimisation campaign reported in [8], which also guided the design of the baffles indicated in fig. 6.

3. Divertor cooling circuit CFD analysis

The thermal-hydraulic performances of the single-circuit cooling option divertor was assessed by running steady-state thermally coupled fluid-structure CFD analysis, under coolant operative conditions and thermal loads summarized respectively in table 1 and table 2. In particular, the compliance with the following constraints [9] was assessed:

- maximum Eurofer temperature < 550°C;
- coolant total pressure drop < 14 bar;
- coolant local minimum saturation margin > 20°C;
- coolant maximum axial velocity in PFUs cooling channels < 16 m/s;
- minimum CHF margin > 1.4 in PFUs cooling channels, SL and RPs FW channels.

Regarding the last point, it is worth mentioning that the CHF margin is defined as the ratio between the *incident* CHF, a definition of which can be found in [10], and the actual heat flux on the plasma-facing walls.

Table 1: Summary of coolant operative conditions.

	Operative Conditions
Inlet Pressure [bar]	70
Inlet Temperature [°C]	130
G per Cassette [kg/s]	36.00

The selected operating conditions come from extensive parametric analysis campaigns [8, 11] which led to the use of different cooling parameters, reported in table 1, with respect to the ones used in previous studies for PFC and CB cooling circuits [12, 13].

More in detail, the choice of the optimal coolant operating conditions is pivotal to meet the different requirements of the single-circuit cooling option divertor, which must simultaneously be able to provide a sufficient cooling potential to allow the PFCs to survive the outstanding plasma heat loads (thus requiring a low coolant temperature, high inlet pressure and high mass flow rate) and ensure a small pressure drop and a high temperature in Eurofer (requiring a low coolant mass flow rate and a high inlet temperature) for the cassette. In particular, this latter condition is required to increase the divertor lifetime, affected by neutron irradiation, which causes embrittlement and reduction of strength, and is dependent on the component operating temperature [1, 14].

A coolant inlet temperature of 130°C and an inlet pressure of 70 bar were selected as trade-off values, based on the outcomes of the parametric analysis campaigns, to be compared to 130°C and 50 bar previously adopted for the PFCs cooling circuit [13], and 180°C and 35 bar of the CB cooling circuit [12]. It is moreover important to emphasise how the 70 bar inlet coolant pressure choice was dictated solely for further improving the CHF margin of the VTs and, therefore, its actual adoption requires detailed studies to assess the structural integrity of the cassette and of the welds to be performed, and eventually to revise the divertor design.

Table 2: Deposited power breakdown for each cassette.

Volumetric Heat Loads	
Component	**Power [MW]**
SL Armour	0.095
SL Structure	1.032
SL Coolant	0.430
RPs Armour	0.024
RPs Structure	0.085
RPs Coolant	0.041
CB Structure	0.547
CB Coolant	0.169
NSs Structure	0.025
NSs Coolant	0.005
VTs Armour	0.519
VTs Structure	0.597
VTs Coolant	0.137
TOTAL	**3.707**
Surface Heat Loads	
Component	**Power [MW]**
SL Surface	0.771
RPs Surface	0.062
VTs Surface	2.430
TOTAL	**3.263**

Concerning the mass flow rate reported in table 1, this was selected on the basis of preliminary fluid-dynamic analyses [8], which estimated 36 kg/s as the maximum value that could be used to achieve a pressure drop slightly below the 14 bar limit, in order to guarantee the VTs maximum coolant velocity and, consequently, obtain the maximum CHF margin achievable. This mass

flow rate value is higher than that previously used for the CB cooling circuit (≈31 kg/s, [12]) and significantly lower than that previously adopted for the PFCs cooling circuit (≈99 kg/s, [13]).

With regard to the heat loads considered, whose breakdown is summarized in table 2, the nuclear contributions were calculated by ENEA Frascati Neutronics Team for the 2021 divertor design [15] and are depicted in fig. 7, while the surface heat loads were drawn from [16]. The resulting temperature increase between inlet and outlet of the divertor cooling circuit, not considering the radiative thermal losses to the VV, amounts to approximately 46°C.

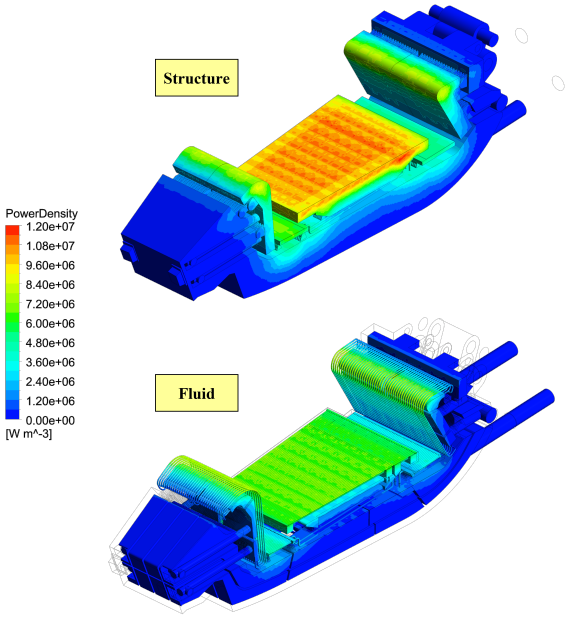

Figure 7: Nuclear heating distribution adopted for calculations.

3.1. Optimal computational mesh selection

The thermofluid-dynamic simulation of the divertor complex cooling circuit with 3D-CFD tools results difficult due to the multiscale nature of its geometry, characterized by an overall length of more than 4 m, and features around 400 channels with diameters of the order of ≈1 cm.

It is therefore evident how it is of paramount importance to select an optimal mesh size, which must be sufficiently fine to guarantee the mesh-independence of the engineering quantities of interest (e.g. the coolant total pressure drop and the maximum temperatures that various materials reach), and at the same time it should be manageable in terms of overall computational cost.

Therefore, mesh-independence analyses were carried out on the individual divertor components and, where it was not possible to guarantee reliable results with the available computational resources (or simply to realize the required meshes), simplifications and modelling choices were made in order to reduce the computational burden while keeping the quality of the results under control, although an inevitable loss of information is obtained.

3.1.1. PFU assembly modelling

The most demanding components from the point of view of computational burden are the PFUs and their supports, which are composed of different materials, have very small geometric details and are subject to high thermal fluxes, which require a sufficient number of cells to correctly reconstruct the thermal gradients that develop. Moreover, on the basis of the mesh-independence analyses of the OVT mock-up cooling circuit, discussed in [17], it can easily be deduced that the complete simulation of the two VTs is even impracticable for the water domain itself, not considering the details of the PFU structures and their supports.

It was therefore decided to renounce the simulation of these components, analysing only the fluid-dynamic aspect through the use of properly calibrated porous media. Using this methodology, the possibility of predicting the thermal field within the PFUs and their supports is lost. However, by identifying the most critical region of VTs, detailed thermofluid-dynamic analyses can be carried out in future works using a sub-modelling approach, adopting the results of the entire cassette as boundary conditions for a single PFU assembly simulation.

To define suitable equivalent porous media, the workflow detailed in the following was adopted. At first, a detailed simulation of the flow field inside the individual PFUs channel was carried out for each of the two targets considering a 0.6 mm bulk size mesh in line with the requirements described in [17]. The mass flow rate was also considered in the range of ±20% from its average nominal value, calculated as the ratio between the total mass flow rate and the number of PFU assemblies. Then, an equivalent fluid domain with no swirl tape was created for each target, adopting a coarser mesh with a bulk size of 1.3 mm, and inserting a porous medium in the entire channel section originally hosting the swirl tape. The equivalent porous media were then calibrated to ensure that the $\Delta p(G)$ curve was reproduced with a very small relative error (less than 3% at the lower mass flow rates), optimising their coefficients using the ANSYS DesignXplorer optimization tool [18]. The com-

parison between the complete model and the equivalent porous medium results is shown in fig. 8.

It is important to remark that this modelling strategy reduces the number of finite volumes for each PFUs channel from about $5 \cdot 10^6$ to $\approx 7 \cdot 10^5$.

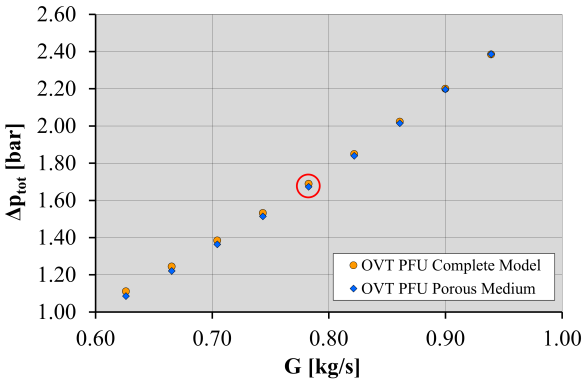

Figure 8: Comparison between complete OVT PFUs channel and porous medium results. The average nominal mass flow rate is circled in red.

It has to be pointed out that the ability to reconstruct the pressure drop curve as a function of G over a fairly wide range of values around the nominal one allows to have some confidence in the distribution of flow rates between the various PFUs channels when the complete simulation is performed, being the equivalent model capable of dealing with deviations from nominal values. Furthermore, the small temperature variations observed in the VTs (in the order of 10°C) reasonably allow to avoid the adoption of temperature corrections.

Finally, in order to correctly reproduce the PFUs energy balance into account, a uniform volumetric heat source was considered for the porous media, being equal to the sum of surface and volumetric contributions detailed in table 2.

3.1.2. Mesh independence studies

For all components except PFUs, the optimal mesh size to be adopted to obtain fairly grid-independent results was assessed through dedicated mesh-independence studies. Several parametric analyses were carried out separately on the individual components, being a complete mesh-independence assessment of the entire divertor too much computationally expensive to be performed. This resulted in a total of more than 50 3D-CFD steady-state thermofluid-dynamic simulations of the SL, inner RP, OVT TB, and CB under realistic operating conditions, allowing moreover to define optimum local mesh sizes for each component in a much more flexible manner. Moreover, for the outer RP and IVT TB, it was assumed that they could be meshed with computational grids with the same features of those adopted respectively for the inner RP and OVT TB.

The analyses were carried out using the Grid Convergence Index (GCI) [19] as a figure of merit, evaluating the Richardson extrapolated values ϕ_0 for a generic quantity ϕ by means of a least-square approach [20]. The GCI was calculated according to the definition of eq. (1), conservatively considering a safety factor $F_s = 3$.

$$GCI = F_s \left| \frac{\phi - \phi_0}{\phi} \right| \tag{1}$$

This approach was applied to several engineering integral quantities of interest for each component, namely the total coolant pressure drop, together with the maximum and average temperatures for each solid region.

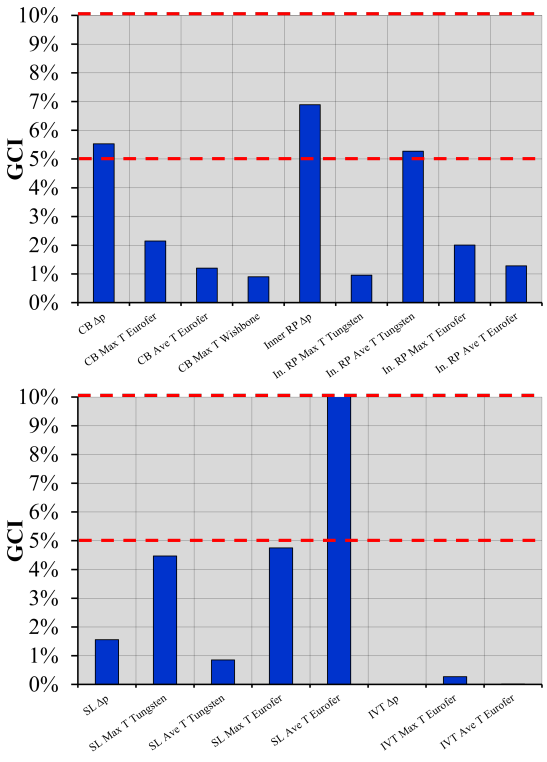

Figure 9: Summary of the GCI values obtained by the preliminary mesh independence analyses.

The results obtained from these analyses are briefly summarized in fig. 9, from which it is interesting to note that the GCI value is always less than 7%, with the only exception of the average Eurofer temperature in SL. For this component, in fact, a grid refinement of

the solid was carried out until meshes of over 180 million volumes were achieved, without being able to obtain a clear convergence trend that could justify a mesh-independent result. This outcome can be explained by the fact that the total number of cells in the SL is mainly dictated by automatic local refinements due to curvatures and proximities, thus distorting the results of the analysis, together with disturbances introduced by the mapping between the different solid and fluid meshes at their interfaces. Nevertheless, variations in average and maximum temperatures of the order of 10°C were obtained in Eurofer and no significant changes in the thermal field features are observed. Therefore, it was decided to avoid further mesh-independence studies of the SL and a computational mesh of intermediate size (10 mm) was selected.

3.1.3. Complete assembled mesh

Once the optimal grid sizes were selected for each component, an overall mesh was assembled, the details of which are depicted in fig. 10 and fig. 11, while its main parameters are summarized in table 3.

Concerning table 3, it is worth noting how the average mesh quality metrics are within the acceptable ranges prescribed in [6] and less than 1% of the overall number of cells is characterized by poor metrics. Consequently, the results are not expected to be significantly influenced by the mesh quality.

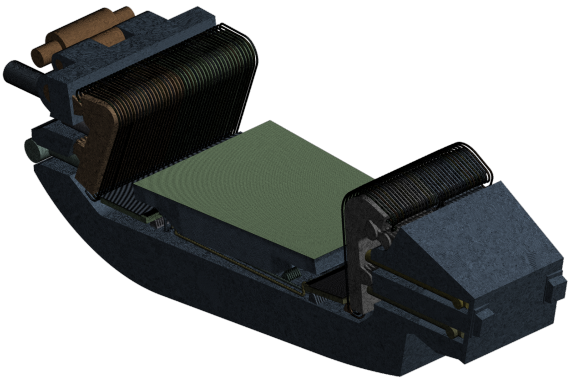

Figure 10: Mesh adopted for the thermofluid-dynamic CFD analysis.

Due to the large size of the computational domain, which counts 120 million nodes and 245 million volumes, it was necessary to rely on the computational resources of the CRESCO/ENEAGRID High Performance Computing infrastructure [21] to perform the thermofluid-dynamics simulations.

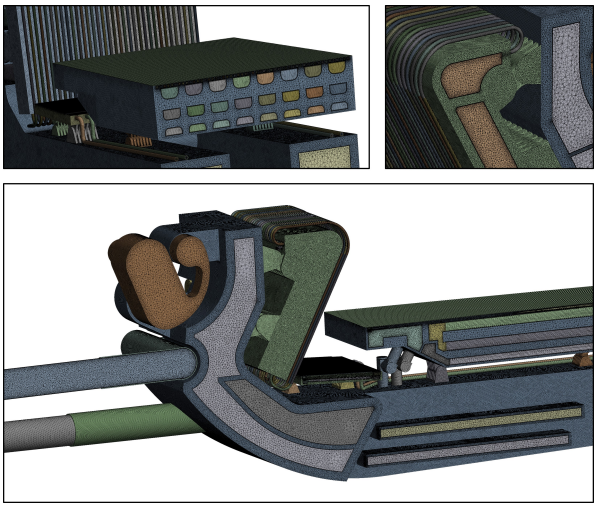

Figure 11: Details of the complete computational mesh.

Table 3: Summary of the main mesh parameters.

Region	Mesh Parameter	Value
Fluid	**Mesh Type**	Hybrid
	Nodes	$9.51 \cdot 10^7$
	Elements	$1.34 \cdot 10^8$
	Inflation Layers Number	12
	First Cell Height [μm]	20 – 50
	Layers Growth Rate	1.2 – 1.35
	Target Element Size [mm]	1.3 – 10
	Surface with y^+>200 [%]	0.01
Structure	**Mesh Type**	Hybrid
	Nodes	$2.48 \cdot 10^7$
	Elements	$1.11 \cdot 10^8$
	Target Element Size [mm]	2.5 – 10
Quality	**Orthogonality Factor (ave/min)**	0.80/0.01
	Expansion Factor (ave/max)	2.98/7597
	Aspect Ratio (ave/max)	15/1427

3.2. Results

The steady-state thermal-hydraulic performances of the divertor cooling circuit under the operative conditions of table 1 were assessed in terms of:

- coolant total pressure and total pressure drop distributions;
- mass flow rate branching between SL and RPs;
- coolant flow velocity distribution among SL, RPs, PFUs and NSs channels;
- coolant temperature and sub-cooling margin distributions;
- CHF margin distribution among SL, RPs, and PFUs channels;
- structure temperature field.

The simulation was carried out considering the assumptions, models and BCs summarised in table 4. Moreover, in order to avoid over-conservative evaluations of the cassette temperature distribution, a radiative heat transfer condition with the VV was considered, this latter supposed to operate at 40°C [22].

Table 4: Summary of assumptions, models and BCs.

Analysis Type	Steady-state coupled thermal analysis
Material Library	Water IAPWS IF97 [23] Eurofer [24] W / Ti6Al4V [25]
Liner / RPs Heat Flux	Uniform according to table 2
Nuclear Heating	From [15]
Radiative Heat Transfer	Towards VV @ 40°C
Turbulence Model	k-ω SST
Boundary Layer Modelling	Automatic Wall Functions
PFU Assembly Modelling	Equivalent porous medium
Wall Roughness	15 μm
Wall Roughness PFUs channels	2 μm
Inlet BC	T=130°C / p_{tot}=70 bar
Outlet BC	G=36.00 kg/s

The analysis ran until all the residuals reached the iteration convergence control criterion of 10^{-4} and a second-order accurate numerical scheme was selected, as suggested by [26]. The CFD simulation required about 38 hours of calculation time to perform 1300 iterations on the ENEA CRESCO cluster, running on 240 Intel Xeon Platinum 8160 processors @2.10 GHz, equipped with a total of 960 GB of RAM.

The main results obtained are reported in the following sections.

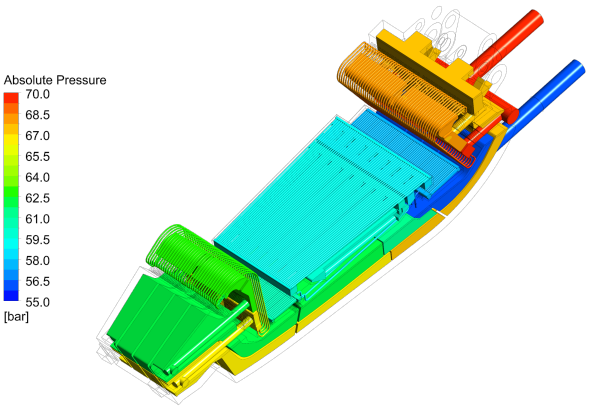

Figure 12: Divertor coolant absolute pressure field distribution.

Pressure drop and pumping power

Coolant pressure distribution and total pressure drop for the main CB components, adopting the nomenclature depicted in fig. 4, are shown in fig. 12 and table 5, respectively, while the calculated mass flow rate branching between SL and RPs cooling circuit is reported in table 6.

As it may be argued from the results, the divertor cooling circuit overall total pressure drop amounts to ≈13.7 bar, being slightly lower than the prescribed limit of 14 bar, as anticipated in section 3. The components with the highest pressure loss are the VTs, due to the presence of the swirl tapes, and the SL, due to the FW channels and the S-shaped inlet and outlet pipes.

Table 5: Coolant total pressure drop distribution.

Divertor Component	**Δp [bar]**
Inlet CB	0.058
OVT	2.233
CB1	0.243
Lower NS	0.703
CB2	0.209
IVT	4.267
CB3	0.406
Upper NS	0.453
CB4	0.210
SL	4.630
Inner RP	1.559
RPs Manifold	1.8420
Outer RP	1.315
Outlet CB	0.590
Total	**13.713**

Table 6: Divertor cooling circuit mass flow rate distribution.

Sections	**G [kg/s]**	**G/G$_{tot}$**
SL	27.95	77.6%
RPs	8.05	22.4%
Total	36.00	-

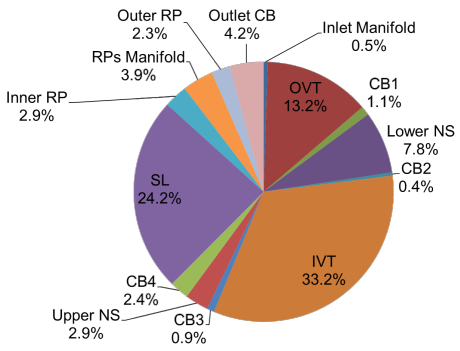

Figure 13: Divertor cooling circuit pumping power breakdown.

By combining the information on pressure drop and flow distribution, it is possible to calculate the required pumping power for each component, a breakdown of which is shown in fig. 13, while the total pumping power required for each cassette amounts to 41.95 kW.

Figure 13 highlights how the two VTs are responsible for the higher coolant pumping losses, together amounting to almost 50% of the total value, SL for ≈24%, the entire RP system for 9%, the two NSs for the 11%, while the CB only for 9%.

The latter results, together with those of table 5 reporting the pressure drop distribution, highlight that the potential for reducing the total pressure drop is limited, as it is significantly influenced by the presence of VTs, for which it is not possible to significantly change the design. Consequently, if an optimisation of the hydraulic circuit aimed at reducing pressure losses is attempted, it would be necessary to revise the SL cooling circuit, being characterized by high losses, then to adjust the RPs, so to rebalance the mass flow rate partition with the SL. In particular, it would be necessary to act on the pipework connecting the CB with these components, as well as to revise their manifolds, since both the BC and FW channels cannot be significantly changed to preserve their capability to handle the plasma heat loads.

Coolant distribution

As far as the coolant distribution is concerned, in the following are reported the results relevant to axial velocity distributions among SL and RPs FW channels (fig. 14 and 15), PFUs channels (fig. 16), and NSs channels (fig. 17).

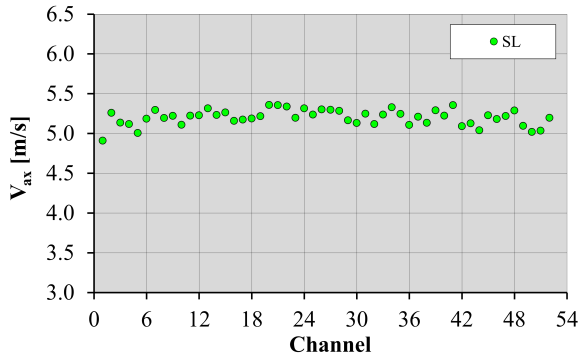

Figure 14: Coolant axial flow velocity distribution among SL FW channels.

With regard to all the components that have toroidal-parallel channels, i.e SL, RPs, and VTs, they are numbered in a clockwise direction looking at the tokamak from above. The NSs channels instead are indicated with a letter representing the two separate cooling circuits for each NS, while the channels are numbered from inlet to outlet, thus resulting from outboard to inboard for the lower NS, and the opposite for the upper NS. Moreover, also concerning the NSs numbering, 1 to 10 are inlet channels, while 11 to 20 are outlet channels.

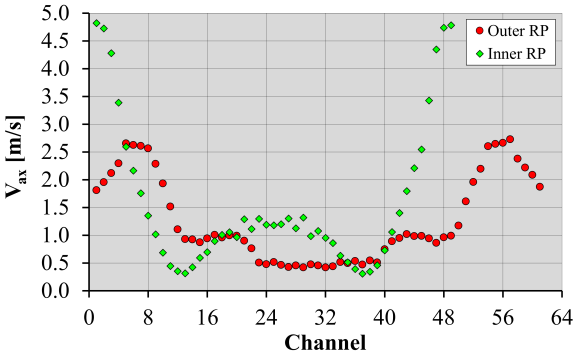

Figure 15: Coolant axial flow velocity distribution among RPs FW channels.

From the analysis of the obtained results, it may be argued that within the SL FW channels the distribution of coolant axial flow velocity is acceptably uniform, with maximum deviations of ±6% with respect to the average value. The distribution of coolant axial velocity, and consequently the mass flow rate, is also quite uniform for the PFUs channels, for which maximum deviations in the range of ±4% from the average values are observed.

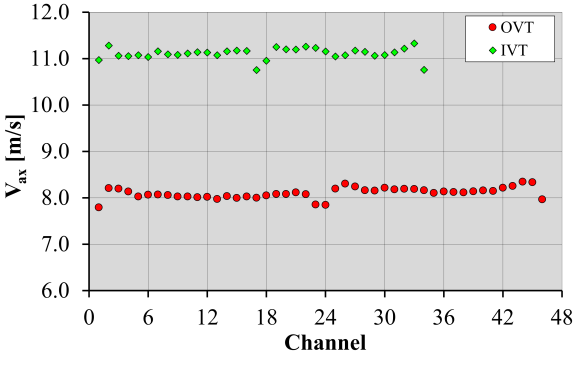

Figure 16: Coolant axial flow velocity distribution among PFUs channels.

Additionally, it can be noted from fig. 16 that the maximum axial velocity constraint in the PFUs channels is met, being the velocities lower than the limit

value of 16 m/s. It should also be noted that the reported velocity has been appropriately scaled to account for the presence of swirl tapes, which are not geometrically modelled using the equivalent porous medium approach.

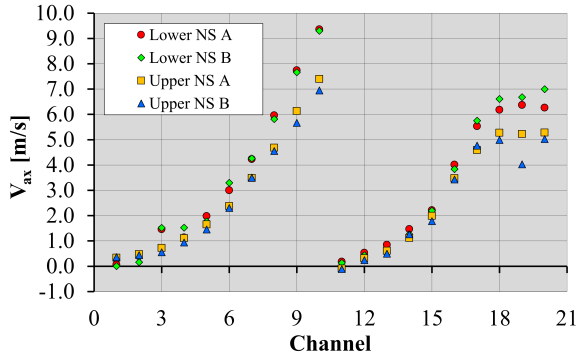

Figure 17: Coolant axial flow velocity distribution among NSs channels.

Completely different results are observed for the RPs FW channels and for the NSs channels, the latter even characterised by flow reversal phenomena. Despite the coolant distribution is not optimal, the results of the thermal analysis reported in the next sections show that no bulk vaporisation phenomena or thermal hot spots in the structures occur. Consequently, the current design of NSs and RPs cooling circuits can be accepted, at least as far as solely thermal aspects are concerned.

Fluid temperature and saturation margin distributions

The coolant temperature distribution is depicted in fig. 18, while the coolant margin against saturation, defined as $T_{sat}(p) - T$ where $T_{sat}(p)$ is drawn from [27], is shown in fig. 19.

As it may be argued from fig. 18, several hot spots occur in the fluid, due to the occurrence of local stagnation caused by some geometrical features of the cassette.

Nevertheless, differently from the 2019 divertor design [12] characterized by localized boiling phenomena, no vaporization is predicted in the fluid domain, with always positive margins against saturation, due to the increased coolant operating pressure and the reduced inlet temperature.

It follows that the constraint on the minimum margin against saturation is respected, being the local minimum value obtained from the simulation $\approx 48°C$, while the value at the outlet of the entire divertor cooling circuit is approximately 95°C.

Moreover, although not visible from the figures, no thermal hot spots are observed for the NSs, despite the

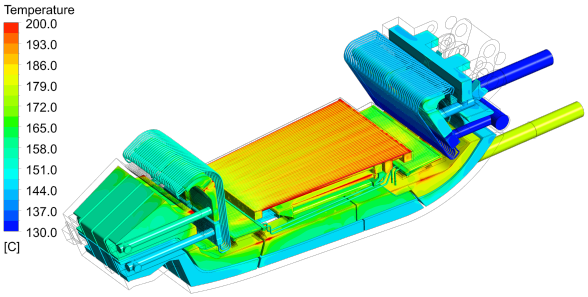

Figure 18: Divertor coolant temperature field.

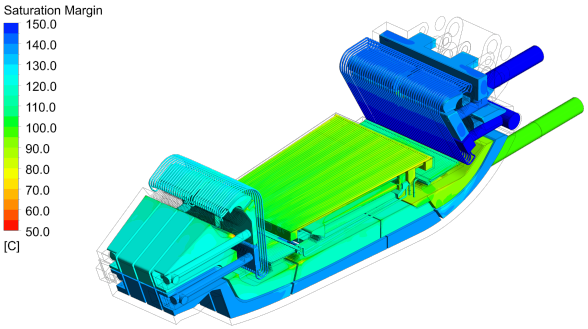

Figure 19: Divertor coolant margin against saturation field.

presence of the highly uneven flow distribution shown in fig. 17. This is due to the low volumetric thermal loads to which these components are exposed, that can be handled even with very low fluid velocities.

CHF margins

The distributions of the margin against CHF onset within the SL FW, RPs FW and PFUs channels were assessed adopting a different approach for the different components in order to check whether its prescribed minimum value of 1.4 is guaranteed by the current cooling circuit design.

As far as the PFUs channels are concerned, the modified Tong-75 correlation given in [10] and already employed in [12, 13] is adopted, considering a maximum heat flux of 20 MW/m^2 as prescribed in [1].

The results obtained are depicted in fig. 20, and clearly shows CHF margins too low to meet the threshold value of 1.4, indicated by the dotted line, being the minimum CHF margins equal to 1.33 and 1.23 respectively for the IVT and the OVT.

When compared to the performances of the 2019 divertor [13], it can be argued that this result is mainly due to the significantly lower velocities in the PFUs channels, which are here equal to around 8 and 11 m/s for

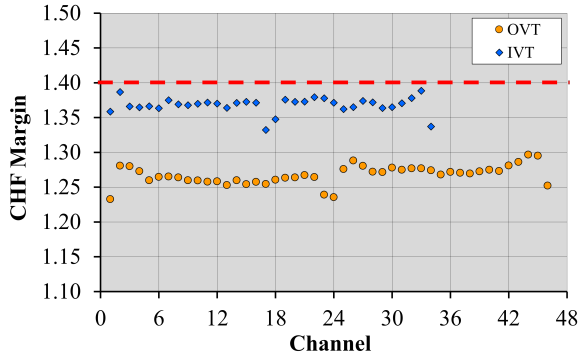

Figure 20: CHF margin distribution among PFUs channels.

OVT and IVT respectively, compared to 14 and 13 m/s for the 2019 configuration. However, increasing these velocities is not a viable strategy, as it would cause an increase in pressure drop of the entire cooling circuit, overcoming the 14 bar maximum pressure drop constraint.

As for the CHF margin for SL and RPs FW channels, these were calculated starting from the CHF look-up tables of [28]. Design peak heat flux values of 1 MW/m^2 and 0.2 MW/m^2 were used according to the indications given in [1] respectively for the FW channels of SL and RPs, while conservative peaking factors f_p values extracted from the CFD simulation were selected for SL and RPs.

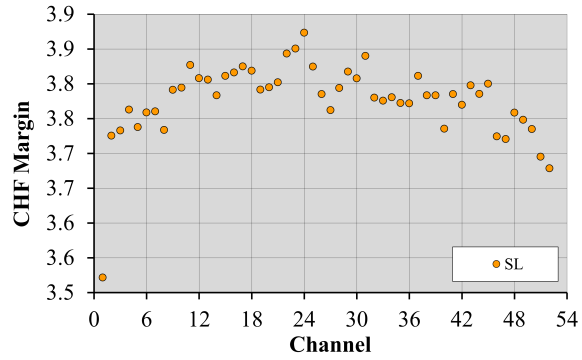

Figure 21: CHF margin distribution among SL FW channels.

The results relevant to the SL FW channels are depicted in fig. 21, calculated with a peaking factor of ≈2.9, while those of the RPs FW channels are shown in fig. 22, calculated with a peaking factor of ≈3.6. It must be pointed out that such high f_p values are only observed at the first and last channels of the FW, which generally experiences higher heat fluxes due to the geometric features of these components, characterized by a toroidal distance between the extreme channels and the side walls of SL and RPs greater than the pitch between two adjacent channels. However, despite the CHF margins are calculated with very conservative values of f_p, they always remain well above the prescribed limit of 1.4 in every single channel.

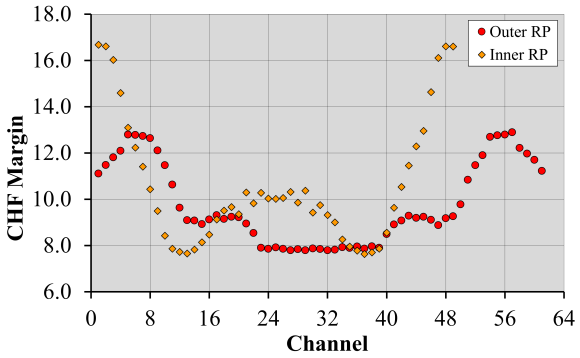

Figure 22: CHF margin distribution among RPs FW channels.

Structure temperature distribution

Finally, the structure temperature field is reported in fig. 23 with a focus on the range that extends from 130°C (the coolant inlet temperature) to 550°C, where the regions in grey are those in which temperatures exceeding 550°C are predicted.

As can be seen from the figure, unduly high temperatures in the structure are observed in SL, IVT supports, and wishbone. Regarding the SL, the maximum temperature reaches a value of 566°C, whose position is circled in fig. 24. As can be argued from these results, the SL cooling circuit layout can be possibly optimised by moving the SL level 3 BCs towards the cassette by few millimeters.

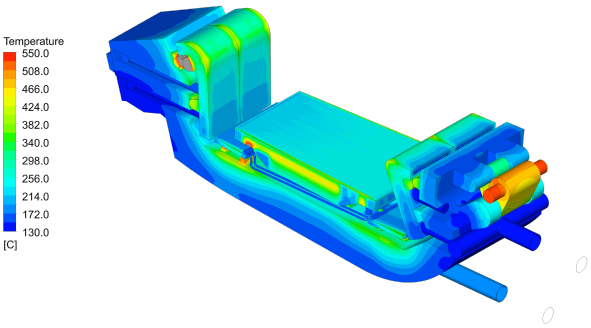

Figure 23: Divertor structure temperature field.

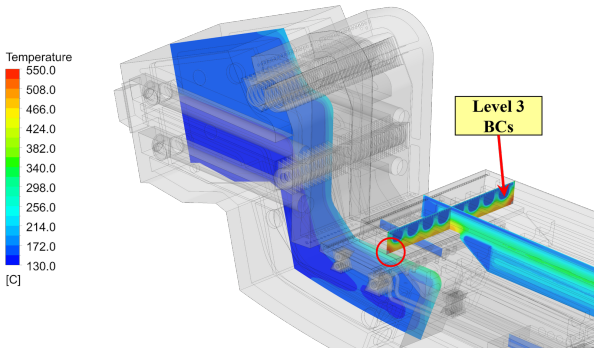

Figure 24: Detail of temperature distribution in SL and position of the thermal spot with respect to level 3 BCs.

As far as the wishbone is concerned, it reaches quite high temperatures as it is not provided with a cooling circuit. The maximum calculated temperature is 547°C, but as can be seen from fig. 23, this is strongly influenced by the boundary conditions used for the simulation. A correct estimation of the temperature distribution in this component would in fact require modelling not only the cassette, but also the outer fixation rail and the main components with which radiative heat exchange phenomena are established (VV and Blanket), with a consequent increase in the computational cost that would make it impossible to carry out the simulation.

Finally, regarding the IVT, a maximum of ≈680°C is reached, and a very large area of the upper supports is working at temperatures above 550°C, as visible in grey in fig. 25. It can be argued from the results that a deep revision of the design of the IVT and its supports is mandatory: in fact, it is probably not sufficient to just reduce the length of the upper supports, to decrease the distance to the heat sinks, but also to increase the thickness of the IVT TB, improving its neutron shielding performance.

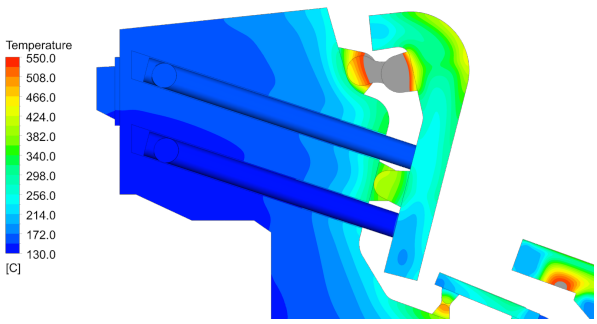

Figure 25: Detail of temperature distribution in IVT supports.

4. Conclusions

The University of Palermo, in collaboration with ENEA and within the framework of the activities promoted by the EUROfusion consortium, carried out a research campaign focussed on the preliminary thermofluid-dynamic assessment of the EU-DEMO divertor single-circuit cooling option under steady-state conditions. A theoretical-numerical approach based on the finite volume method was followed and the ANSYS CFX code was adopted, while the simulations were made possible by the use of the CRESCO High Performance Computing infrastructure.

The divertor thermal-hydraulic performances were assessed in terms of coolant and structure temperature, coolant total pressure drop, flow velocity distribution, and CHF margin for SL, RPs, and PFUs cooling channels.

The results obtained highlighted some important shortcomings of the single-circuit cooling option design, namely the occurrence of thermal hot spots in SL, wishbone and IVT supports (with Eurofer temperatures up to 680°C), and the occurrence of CHF margins remarkably smaller than 1.4 for every PFUs channel, thus resulting in significantly worse thermal-hydraulic performances than the 2019 double-circuit option.

Although it is easy to identify a set of design review actions for the divertor cooling circuit that would eliminate or mitigate the occurrence of the thermal hot spots, it remains doubtful whether a solution can be found that can simultaneously ensure compliance with the CHF margin requirements in VTs and the total pressure drop of the cooling circuit without resorting to a reduction of the coolant inlet temperature and/or a further increase in operating pressure, which would entail a reduced component lifetime and potential issues for the structural integrity of cassette and welds.

In fact, an improvement of the CHF margins can indeed be achieved by increasing the coolant mass flow rate, but this rise would result in a significant growth in pressure drop. It follows that a further revision of the cooling circuit design aimed at reducing the hydraulic pressure drop and increase the heat transfer performance has to be investigated.

CRediT authorship contribution statement

A. Quartararo: Conceptualization, Methodology, Investigation, Writing - original draft. **S. Basile**: Conceptualization, Methodology, Investigation, Writing - original draft. **F.M. Castrovinci**: Conceptualization, Methodology, Investigation, Writing - original draft.

P.A. Di Maio: Conceptualization, Methodology, Investigation, Writing - original draft. **M. Giardina**: Conceptualization, Methodology, Investigation, Writing - original draft. **G. Mazzone**: Conceptualization, Methodology, Investigation, Writing - original draft. **E. Vallone**: Conceptualization, Methodology, Investigation, Writing - original draft. **J.H. You**: Conceptualization, Methodology, Investigation, Writing - original draft.

Declaration of Competing Interest

The authors declare that they have no known competing financial interests or personal relationships that could have appeared to influence the work reported in this paper.

Acknowledgments

This work has been carried out within the framework of the EUROfusion Consortium, funded by the European Union via the Euratom Research and Training Programme (Grant Agreement No 101052200 — EUROfusion). Views and opinions expressed are however those of the author(s) only and do not necessarily reflect those of the European Union or the European Commission. Neither the European Union nor the European Commission can be held responsible for them.

The computing resources and the related technical support used for this work have been provided by CRESCO/ENEAGRID High Performance Computing infrastructure and its staff [29]. CRESCO/ENEAGRID High Performance Computing infrastructure is funded by ENEA, the Italian National Agency for New Technologies, Energy and Sustainable Economic Development and by Italian and European research programmes, see [21] for information.

References

[1] J.H. You, et al., Divertor of the European DEMO: Engineering and technologies for power exhaust, Fusion Engineering and Design 175 (2022) 113010. doi:https://doi.org/10.1016/j.fusengdes.2022.113010.

[2] T. Donné, W. Morris, European Research Roadmap to the Realisation of Fusion Energy, 2018, ISBN: 978-3-00-061152-0.

[3] G. Federici, et al., Overview of the DEMO staged design approach in Europe, Nuclear Fusion 59 (2019) 066013. doi:10.1088/1741-4326/ab1178.

[4] G. Federici, J. Holden, C. Baylard, A. Beaumont, The eu demo staged design approach in the pre-concept design phase, Fusion Engineering and Design 173 (2021) 112959. doi:https://doi.org/10.1016/j.fusengdes.2021.112959.

[5] D. Marzullo, V. Imbriani, F. Giovanna, DIV-DEMO.S.1-T001-D001_DEMO Divertor CAD model 2021, 2021, EUROfusion IDM Ref.: 2PHRQZ v1.0.

[6] ANSYS Inc., ANSYS CFX-Solver Theory Guide, 2021, Release: 2021 R1.

[7] M. Merola, et al., Overview and status of ITER internal components, Fusion Engineering and Design 89 (7) (2014) 890–895. doi:10.1016/j.fusengdes.2014.01.055.

[8] P.A. Di Maio, DIV-DEMO.S.1-T002-D001_Divertor Thermo-hydraulic assessment 2021, 2022, EUROfusion IDM Ref.: 2PHWSW v1.0.

[9] G. Mazzone, et al., Eurofusion-DEMO Divertor - Cassette Design and Integration, Fusion Engineering and Design 157 (2020) 111656. doi:10.1016/j.fusengdes.2020.111656.

[10] A.R. Raffray, et al., Critical heat flux analysis and R&D for the design of the ITER divertor, Fusion Engineering and Design 45 (4) (1999) 377–407. doi:10.1016/S0920-3796(99)00053-8.

[11] P.A. Di Maio, et al., DIV-1-T007-D006 - Divertor Thermo-hydraulic assessment 2020, 2021, EUROfusion IDM Ref.: 2P6AMZ v1.0.

[12] P.A. Di Maio, et al., Thermal-hydraulic study of the DEMO divertor cassette body cooling circuit equipped with a liner and two reflector plates, Fusion Engineering and Design 167 (2021) 112227. doi:https://doi.org/10.1016/j.fusengdes.2021.112227.

[13] P.A. Di Maio, et al., Hydraulic assessment of an upgraded pipework arrangement for the DEMO divertor plasma facing components cooling circuit, Fusion Engineering and Design 168 (2021) 112368. doi:https://doi.org/10.1016/j.fusengdes.2021.112368.

[14] G. Mazzone, et al., Choice of a low operating temperature for the DEMO EUROFER97 divertor cassette, Fusion Engineering and Design 124 (2017) 655–658. doi:https://doi.org/10.1016/j.fusengdes.2017.02.013.

[15] R. Villari, DIV-DEMO.S.1-T003-D001_Neutronics and shielding assessment report 2021, 2022, EUROfusion IDM Ref.: 2PJ33J v1.0.

[16] E. Vallone, et al., Conference Paper. Thermal-hydraulic study of the Primary Heat Transfer System of EU-DEMO Divertor Plasma Facing Components, The 19 th International Topical Meeting on Nuclear Reactor Thermal Hydraulics (NURETH-19) Brussels, Belgium, March 6 - 11, 2022, ISBN 9789076971261, 2022.

[17] A. Tincani, et al., Hydraulic Characterization of the Full Scale Mock-Up of the DEMO Divertor Outer Vertical Target, Energies 14 (23) (2021). doi:10.3390/en14238086.

[18] ANSYS Inc., ANSYS DesignXplorer User's Guide, 2021, Release: 2021 R1.

[19] P. J. Roache, Verification of Codes and Calculations, AIAA Journal 36 (5) (1998) 696–702. doi:10.2514/2.457.

[20] L. Eça, M. Hoekstra, A procedure for the estimation of the numerical uncertainty of CFD calculations based on grid refinement studies, Journal of Computational Physics 262 (2014) 104–130. doi:https://doi.org/10.1016/j.jcp.2014.01.006.

[21] http://www.cresco.enea.it/english.

[22] T. Haertl, et al., Rationale for the selection of the operating temperature of the DEMO vacuum vessel, Fusion Engineering and Design 146 (2019) 1096–1099. doi:10.1016/j.fusengdes.2019.02.014.

[23] International Association for the Properties of Water and Steam, Revised Release on the IAPWS Industrial Formulation 1997 for the Thermodynamic Properties of Water and Steam, 2007.

[24] F. Gillemot and et al., Material Property Handbook pilot project on EUROFER97 (MTA EK, KIT), 2016, EUROfusion IDM Ref.: 2MRP77.

[25] ITER Material Properties Handbook, ITER Document No. G74 MA 16.

[26] J. Mahaffy, et al., Best practice guidelines for the use of CFD in nuclear reactor safety applications, Tech. rep., Organisation for Economic Co-Operation and Development (2007).

[27] P.J. Linstrom, W.G. Mallard, Eds., NIST Chemistry WebBook, NIST Standard Reference Database Number 69 ,National Institute of Standards and Technology, Gaithersburg MD, 20899 (retrieved September 9, 2019). doi:10.18434/T4D303.

[28] D.C. Groeneveld, et al., The 2006 CHF look-up table, Nuclear Engineering and Design 237 (15) (2007) 1909–1922. doi:https://doi.org/10.1016/j.nucengdes.2007.02.014.

[29] F. Iannone, et al., CRESCO ENEA HPC clusters: a working example of a multifabric GPFS Spectrum Scale layout, in: 2019 International Conference on High Performance Computing Simulation (HPCS), 2019, pp. 1051–1052.